
Article:
Bhuva, Montu, Daly, Greg, Hassall, Geoff et al. (2026) Increasing the spatial uniformity of SiO2 films produced by plasma enhanced chemical vapor deposition using capacitively coupled plasmas with structured electrodes. Journal of vacuum science & technology a-Vacuum surfaces and films. 023008. ISSN: 0734-2101

Increasing the spatial uniformity of SiO_2 films produced by plasma enhanced chemical vapour deposition using capacitively coupled plasmas with structured electrodes

Montu P. Bhuva[1,*], Greg Daly[1], Geoff Hassall[1], James Ellis[1], Erik Wagenaars[2], and James P. Dedrick[2]

[1]Oxford Instruments Plasma Technology, Severn Beach, Bristol BS35 4GG, UK

[2]York Plasma Institute, School of Physics, Engineering and Technology, University of York, Heslington, York YO10 5DD, UK

[*]E-mail: montu.bhuva@oxinst.com

January 16, 2026

Silicon dioxide (SiO_2) thin films produced through plasma enhanced chemical vapour deposition are of significant interest for technological applications. Maximising spatial uniformity of the film thickness and refractive index remains challenging for large wafers. In this study, we utilise 2D fluid-kinetic simulations and experiments to investigate the effect of introducing ring-shaped cavities into the showerhead electrode of capacitively coupled plasmas operating at pressures ranging from 1 to 2.2 Torr. Simulations in pure silane (SiH_4) exhibit spatially localised regions of increased electron density and temperature surrounding the electrode cavities, and are used to determine the design of a 'structured' showerhead electrode for comparison with a planar electrode. SiO_2 thin films are experimentally deposited with an industrial reactor operating with a feed gas mixture $SiH_4/N_2O/N_2$ onto 200 mm silicon wafers. Films deposited with the structured electrode are observed to approximately double the film-thickness uniformity for pressures 1.3 to 2.2 Torr while maintaining similar values of the refractive index and process rate.

I INTRODUCTION

Plasma-assisted materials processing is of significant interest to the development of advanced semiconductor technologies[1–3]. This includes the manufacture of integrated circuits[4], solar cells[5], plasma display panels[6], photonics[7], microelectromechanical systems (MEMS)[8] and quantum devices[9].

The ability to generate large-diameter plasmas, i.e. above 30 cm, with a relatively simple electrode configuration makes capacitively coupled plasmas (CCPs) suitable for plasma processing, for example with plasma enhanced chemical vapor deposition (PECVD)[10], sputtering[11] and reactive ion etching[12]. The production of a spatially uniform, large-area plasma is one of the key requirements for processing large substrates[13]. For CCPs, geometric constraints on the plasma chamber often lead to electromagnetic[14–18] and electrostatic effects[19–21] that ultimately result in the spatially non-uniform plasmas. Therefore, the application of CCPs within the semiconductor sector still has some significant challenges to overcome to deliver improved uniformity over larger wafers.

Several techniques have been proposed to enable enhanced control of plasma properties in parallel plate CCP discharges. The majority of these techniques consider the electrical asymmetry effect[22–36] via 'tailored' voltage waveforms consisting of multiple frequency components. The spatial plasma properties can also be controlled by modifying the physical characteristics of the electrodes, including those that are lens shaped[37–39], ladder shaped[40], graded conductivity[41], spatially varying surface material[42,43], radio-frequency (rf) driven electrodes in triode configuration[44] and with the incorporation of cavity structures[45–50]. Hybrid techniques, which are based on both electrical and physical aspects, have also

been demonstrated, including cylindrical electrodes with a transverse magnetic field[51,52], phase-shift control for CCPs with spatially varying material properties[53], structured electrode with multicusp magnetic field topology[54] and application of tailored waveforms to structured electrode CCPs[55].

Previously, Ohtsu *et al.* in Ref. 45–48 demonstrated that a structured electrode cavity can physically alter the radial density profile in CCP discharges under the impact of hollow cathode effect (HCE). Schmidt *et al.* in Ref. 49 studied the impact of different cavity profiles on plasma heating and uniformity. Recently, Wang *et al.* in Ref. 50 reported the effect of incorporating a series of identical cavities on the electron dynamics and plasma uniformity in a parallel plate CCP. All of these investigations were reported for relatively low operating pressures (below 0.5 Torr), where the HCE is primarily dominated by the confinement of energetic secondary electrons within the structural cavities[56]. For PECVD applications it is of significant interest to increase control of spatial plasma uniformity in the intermediate pressure regime, i.e. $\sim$1 Torr.

In this study, we demonstrate the application of structured electrodes in the form of a showerhead to improve the spatial uniformity of SiO_2 thin films that are produced using PECVD. Section II describes the numerical simulations in SiH_4, methods for PECVD experiments, and the diagnostics for measurement of film thickness and refractive index. This is followed by a description of the simulation and experimental results in section III and conclusions in section IV.

II METHODS

A Numerical simulations

Two-dimensional fluid-kinetic simulations are undertaken with the Hybrid Plasma Equipment Model (HPEM)[57]. In this work, HPEM is accessed using a virtual interface Quantemol-VT[58].

1 Simulation geometry

As shown in Figure 1, we investigate two different showerhead configurations. We refer to these as the 'planar' and 'structured' showerheads.

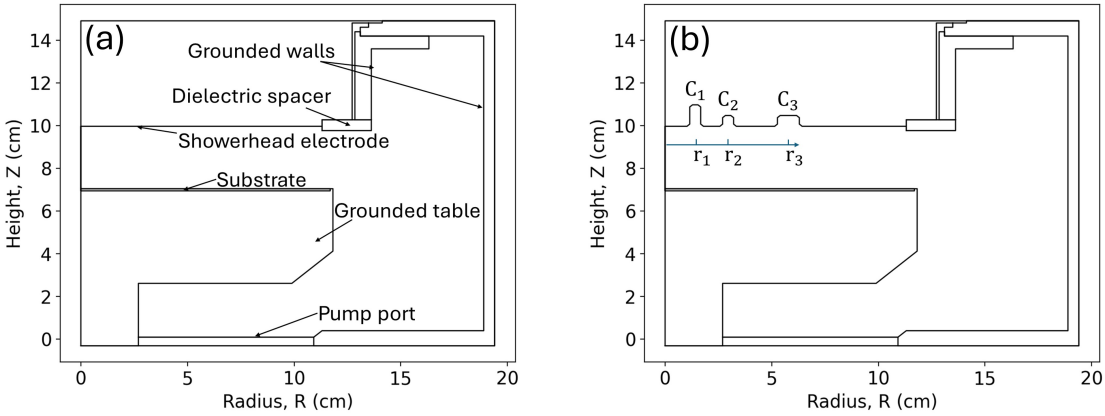

FIG 1. The simulation domain. The capacitively coupled plasma is driven by a radio-frequency powered showerhead electrode. Panels (a) and (b) show the geometry of the planar and structured showerheads, respectively.

The 'planar' showerhead configuration in Figure 1 (a) represents the conventional parallel-plate CCP system. As distinct from this, the structured showerhead, Figure 1 (b), incorporates three annular cavities, named C_1, C_2 and C_3, each with a rectangular cross-section. Their dimensions are summarised in Table I.

TABLE I. Dimensions of the structured showerhead cavities, shown in Figure 1 (b). Each cavity has a rectangular cross-section, defined by its height, h, width, w, and radial position, r, with respect to the central axis of the reactor. Units of cm.

C_1	C_2	C_3
$h_1 = 1$	$h_2 = 0.5$	$h_3 = 0.5$
$w_1 = 0.5$	$w_2 = 0.5$	$w_3 = 1$
$r_1 = 1.25$	$r_2 = 2.75$	$r_3 = 5.5$

For all simulations, the domain has a radius of 19.4 cm and an axial height of 15.2 cm. The mesh consists of a total 152 cells in both the radial and axial directions. This corresponds to a mesh resolution of 1.28 mm per cell in the radial direction and 1 mm per cell in the axial direction. In the simulation model, an external circuit with an rf voltage source and a blocking capacitor is connected to the showerhead electrode (not shown in Figure 1). This circuit blocks the direct current back to the power source and maintains the time-averaged DC self-bias voltage on the powered showerhead electrode.

The geometry of the structured showerhead is determined through a series of parametric studies with numerical simulations, for which the primary metric of interest is the radial uniformity of the total ion flux incident onto the substrate. Simulations were undertaken in a hierarchical fashion with different cavity configurations individually in Ar, O_2 and SiH_4 plasma chemistries to reach the showerhead design shown in Table I.

2 Simulation framework and theory

A detailed description of the hybrid scheme employed in HPEM is available in Ref. 57, and therefore only a summary is provided here. HPEM has a modular structure that enables specific aspects of a given plasma system to be modelled

with different techniques and operating conditions. In this study, we make use of the Electron Energy Transport Module (EETM) and the Fluid Kinetics Poisson Module (FKPM).

Electrons, ions and neutrals are treated as fluids by solving the conservation equations for mass, momentum and energy. The rate coefficients required for the fluid model are determined from the electron energy distribution function (EEDF) by solving the two-term approximation of the Boltzmann equation. Secondary electrons are considered separately and are modelled with a Monte Carlo technique. They are emitted from all plasma-facing metal surfaces with an initial energy of 4 eV and are accelerated according to the local electric field[55]. The secondary electron emission coefficient is 0.1 and is independent of the incident ion energy[55,59]. This is a valid simplification for low-energy ion impact (typically below 50 eV) where most secondary electrons are emitted with energies in the 2–4 eV range[59]. Additionally, all plasma-facing material surfaces, excluding the process substrate and dielectric spacer, are aluminium and modelled with a work function 4.08 eV and a temperature of 298 K.

3 Gas flow and plasma chemistry

The working gas for all simulations is SiH_4. The gas is treated as static and its pressure is held constant at 1.5 Torr. The gas temperature is self-consistently determined with respect to the spatial location.

The SiH_4 chemistry model considered in the simulations includes electrons, ground-state neutrals, excited neutrals, positive ions and negative ions as shown in Table II. The full reaction mechanism is shown in Table III and accessed using Quantemol-DB[60].

TABLE II. Species that are included in the plasma chemistry model.[a,b]

Neutrals	Positive ions	Negative ions	Others
H, H_2, H^*, H_2^*, SiH_2, SiH_3, SiH_4, Si_2H_4, Si_2H_5, Si_2H_6, Si_3H_7, Si_3H_8, Si_4H_9, Si_4H_{10}, Si_5H_{11}, Si_5H_{12}, Si_6H_{13}, Si_6H_{14}, Si_7H_{15}, Si_7H_{16}, Si_8H_{17}, Si_8H_{18}, Si_9H_{20}	H^+, H_2^+, H_3^+, SiH_2^+, SiH_3^+, $Si_2H_4^+$	SiH_3^-	e^-

[a] The wall sticking coefficient for positive ions, negative ions, electrons and excited neutrals H^* and H_2^* is considered as 1.0.

[b] The wall sticking coefficient for all other neutral species is considered as 0.0.

As shown in Table III, reactions R1-R27 refer to electron impact reactions, and R28-R58 refer to the heavy particle reactions.

For electron impact reactions R1-R22 the rate coefficients are determined from the EEDF. The electron collision cross-sections used for these reactions are taken from the references shown in Table III and accessed via the HPEM database. For reactions R23-R27 the rate coefficients are specified using an Arrenhius expression $R = A(T_e^n)\exp(-E/T_e)$, where A is the Arrenhius coefficient (units of cgs), T_e is the electron temperature (units of eV) and E is the activation energy (units of eV). The rate coefficients for heavy species reactions are specified using an Arrenhius expression $R = A(T_0^n)\exp(-E/T_g)$, where A is the Arrenhius coefficient (units of cgs), T_g is the gas temperature (units of K), $T_0 = T_g/298$ and E is the activation energy (units of eV).

TABLE III. Reaction mechanism for the SiH_4 plasma simulations.

No.	Reaction	Rate coefficient	Reference
R1	$e^- + H_2 \rightarrow e^- + H_2$	$f(\epsilon)$	61
R2	$e^- + H_2 \rightarrow e^- + H_2^*$	$f(\epsilon)$	61
R3	$e^- + H_2 \rightarrow e^- + H_2^*$	$f(\epsilon)$	61
R4	$e^- + H_2 \rightarrow e^- + H + H$	$f(\epsilon)$	62
R5	$e^- + H_2 \rightarrow e^- + e^- + H_2^+$	$f(\epsilon)$	62
R6	$e^- + H_2 \rightarrow e^- + H + H^*$	$f(\epsilon)$	63
R7	$e^- + H_2^+ \rightarrow e^- + H_2^+$	$f(\epsilon)$	64
R8	$e^- + H_2^+ \rightarrow e^- + H^+ + H$	$f(\epsilon)$	62
R9	$e^- + H_2^+ \rightarrow H + H$	$f(\epsilon)$	65
R10	$e^- + H \rightarrow e^- + H^*$	$f(\epsilon)$	61
R11	$e^- + H^+ \rightarrow H$	$f(\epsilon)$	66
R12	$e^- + H_3^+ \rightarrow e^- + H_2 + H^+$	$f(\epsilon)$	65
R13	$e^- + H_3^+ \rightarrow H_2 + H$	$f(\epsilon)$	67
R14	$e^- + SiH_4 \rightarrow e^- + SiH_4$	$f(\epsilon)$	66
R15	$e^- + SiH_4 \rightarrow e^- + H + H + SiH_2$	$f(\epsilon)$	66
R16	$e^- + SiH_4 \rightarrow e^- + e^- + H + H + SiH_2^+$	$f(\epsilon)$	66
R17	$e^- + SiH_4 \rightarrow e^- + e^- + H + SiH_3^+$	$f(\epsilon)$	66
R18	$e^- + SiH_4 \rightarrow e^- + SiH_3 + H^*$	$f(\epsilon)$	66
R19	$e^- + SiH_4 \rightarrow e^- + H + SiH_3$	$f(\epsilon)$	66
R20	$e^- + SiH_3^+ \rightarrow e^- + SiH_3^+$	$f(\epsilon)$	68
R21	$e^- + SiH_3^+ \rightarrow H + SiH_2$	$f(\epsilon)$	69
R22	$e^- + SiH_4 \rightarrow H + SiH_3^-$	$f(\epsilon)$	66
R23	$e^- + SiH_4 \rightarrow e^- + H_2 + SiH_2$	$1.6 \times 10^{-7} T_e^{-1} \exp(-11/T_e)$	70
R24	$e^- + SiH_4 \rightarrow e^- + e^- + H_2 + SIH_2^+$	$3.56 \times 10^{-7} T_e^{-1.2} \exp(-16/T_e)$	70
R25	$e^- + Si_2H_6 \rightarrow e^- + H + SiH_3 + SiH_2$	3.72×10^{-10}	66
R26	$e^- + SiH_2^+ \rightarrow SiH_2$	1.13×10^{-13}	69
R27	$e^- + H_2 \rightarrow e^- + e^- + H^+ + H$	$3.00 \times 10^{-8} T_e^{0.44} \exp(-38/T_e)$	71
R28	$SiH_4 + SiH_2^+ \rightarrow SiH_3^+ + SiH_3$	1.07×10^{-9}	66
R29	$H_2^+ + SiH_4 \rightarrow H_2 + H_2 + SiH_2^+$	3.66×10^{-11}	66
R30	$H_2^+ + SiH_4 \rightarrow H_2 + H + SiH_3^+$	6.23×10^{-10}	66
R31	$SiH_3^+ + SiH_3^- \rightarrow SiH_3 + SiH_3$	5.00×10^{-7}	72
R32	$SiH_3^- + Si_2H_4^+ \rightarrow SiH_3 + SiH_2 + SiH_2$	1.00×10^{-7}	72
R33	$SiH_4 + SiH_2^+ \rightarrow H_2 + Si_2H_4^+$	2.50×10^{-10}	73
R34	$H + SiH_4 \rightarrow H_2 + SiH_3$	$2.80 \times 10^{-11} \exp(-1250/T_g)$	69
R35	$SiH_3 + SiH_3 \rightarrow SiH_4 + SiH_2$	1.50×10^{-10}	69
R36	$H_2 + SiH_2 \rightarrow SiH_4$	3.00×10^{-12}	69
R37	$SiH_4 + SiH_2 \rightarrow Si_2H_6$	1.20×10^{-11}	69
R38	$Si_2H_6 + SiH_2 \rightarrow Si_3H_8$	2.60×10^{-11}	69
R39	$H + Si_2H_6 \rightarrow SiH_4 + SiH_3$	1.60×10^{-10}	74
R40	$Si_2H_5 + Si_2H_5 \rightarrow Si_4H_10$	1.50×10^{-10}	69
R41	$H + Si_2H_6 \rightarrow H_2 + Si_2H_5$	$2.40 \times 10^{-10} \exp(1250/T_g)$	69
R42	$H_2 + H^+ \rightarrow H_2^+ + H$	$3.22 \times 10^{-10} \exp(-21856/T_g)$	75
R43	$SiH_2 + Si_3H_8 \rightarrow Si_4H_10$	2.60×10^{-11}	69
R44	$SiH_2 + Si_4H_10 \rightarrow Si_5H_12$	2.60×10^{-11}	69
R45	$SiH_2 + Si_5H_12 \rightarrow Si_6H_14$	2.60×10^{-11}	69
R46	$SiH_2 + Si_6H_14 \rightarrow Si_7H_16$	2.60×10^{-11}	69
R47	$SiH_2 + Si_7H_16 \rightarrow Si_8H_18$	2.60×10^{-11}	69
R48	$SiH_2 + Si_8H_18 \rightarrow Si_9H_20$	2.60×10^{-11}	69
R49	$H + Si_3H_8 \rightarrow H_2 + Si_3H_7$	1.10×10^{-11}	69
R50	$H + Si_4H_10 \rightarrow H_2 + Si_4H_9$	1.10×10^{-11}	69
R51	$H + Si_5H_12 \rightarrow H_2 + Si_5H_11$	1.10×10^{-11}	69
R52	$H + Si_6H_14 \rightarrow H_2 + Si_6H_13$	1.10×10^{-11}	69
R53	$H + Si_7H_16 \rightarrow H_2 + Si_7H_15$	1.10×10^{-11}	69
R54	$H + Si_8H_18 \rightarrow H_2 + Si_8H_17$	1.10×10^{-11}	69
R55	$H_2 + H \rightarrow H + H + H$	$4.67 \times 10^{-7} T_0^{-1} \exp(-55000/T_g)$	76
R56	$H_2 + H_2^+ \rightarrow H_2 + H^+ + H$	$1.00 \times 10^{-8} \exp(-84100/T_g)$	76
R57	$H_2 + H_2^* \rightarrow H_2 + H_2$	1.00×10^{-13}	76
R58	$H_2 + H^* \rightarrow H_2 + H$	1.00×10^{-13}	76

B Experiments in plasma enhanced chemical vapour deposition

1 Plasma source

The experiments are performed in a custom-built capacitatively coupled plasma source, shown in Figure 2.

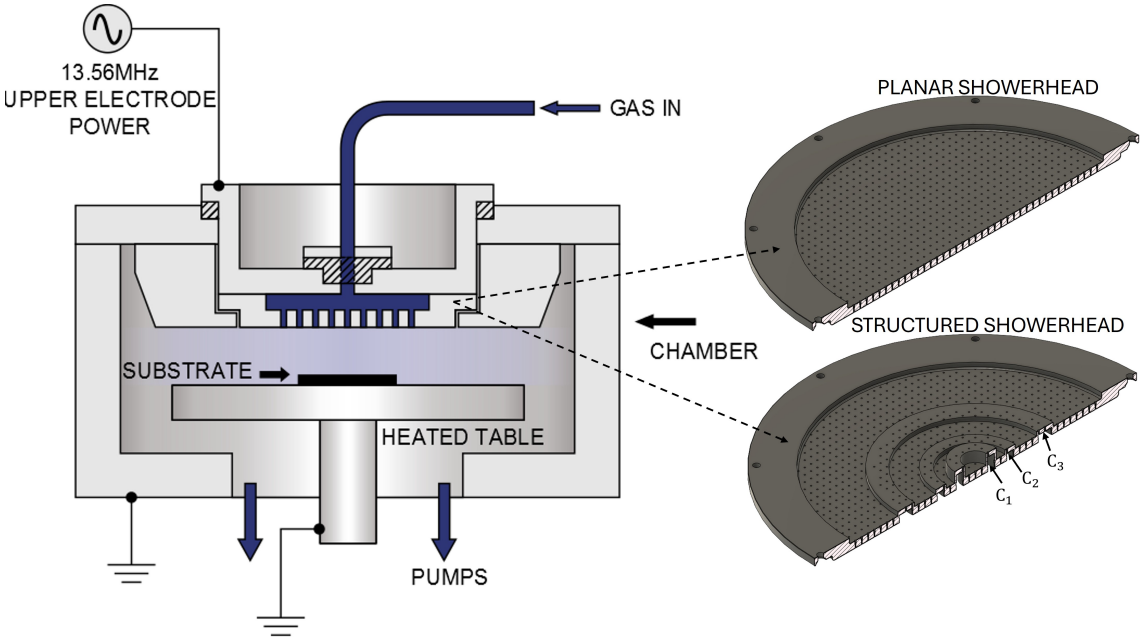

FIG 2. Diagram of the plasma source (Oxford Instruments PP100 PECVD[77]) that is used for the experiments. The dotted arrows show the location where the planar and structured showerheads are separately installed.

The showerhead electrode, through which process gas is introduced to the reactor, is driven by continuous radio-frequency (rf) power at 13.56 MHz. A capacitively coupled plasma is sustained between the powered showerhead and the grounded table electrode. Thin films are chemically deposited on a substrate that is placed on the heated table. Gas is pumped out of the process chamber through a pumping port, which is located under the table.

We investigate the process results arising from two different showerhead electrodes, shown in figure 2. The structured showerhead electrode contains three annular cavities of rectangular cross-section, the dimensions of which are shown in Table I.

2 Deposition process

The deposition of SiO_2 films is carried out in a clean room environment onto 20 cm diameter bare silicon wafers using $SiH_4/N_2O/N_2$ as the process gas at pressures of 1-2.5 Torr. The grounded table electrode is heated to 350°C and the showerhead electrode is powered at 150 W. In this process, N_2 acts as a carrier gas with SiH_4 and N_2O acting as the key reagents for the SiO_2 film growth. The deposition process is carried out on each wafer for 10 minutes, and is followed by a chamber cleaning recipe.

3 Diagnostics for measuring the film thickness and refractive index

The spatial distribution of the film thickness and refractive index is measured using an ellipsometer. Measurements are taken at a series of concentric and linear points spanning the 20 cm diameter as shown in Figure 3.

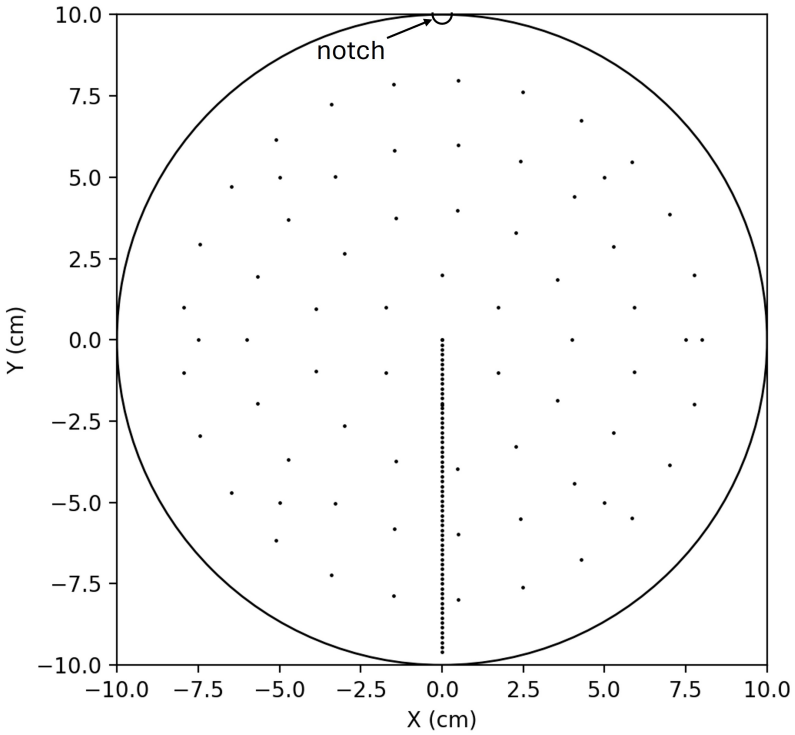

FIG 3. Ellipsometry measurement pattern for determining the spatial variation in the thickness and refractive index of films deposited onto 20 cm diameter wafers.

As shown in Figure 3, the concentric data points cover 15 cm circular diameter of the wafer. The more finely spaced linear data points, opposite the wafer notch, cover the radial extent of 10 cm with a 3 mm edge exclusion. This measurement pattern has been chosen to help identify the difference in film properties for the planar and structured showerhead electrodes.

Spatially resolved measurements of film thickness and refractive index are used to calculate the uniformity parameter U:

$$U = \frac{\max(\mathrm{n_x}) - \min(\mathrm{n_x})}{2 \cdot \mathrm{mean}(\mathrm{n_x})} \cdot 100 \tag{1}$$

In equation 1, $\mathrm{n_x}$ refers to the spatially measured data points shown in Figure 3,

and the subscript x refers to either the film thickness or refractive index. A lower value of the uniformity parameter indicates that the deposited film has a higher degree of radial uniformity for the selected parameter. The average value of the film thickness and process time for the deposition are used to determine the deposition rate.

III RESULTS

A Simulations of the plasma properties in SiH_4

1 Electron density and temperature

Figure 4 shows the spatial electron density and temperature simulated using planar and structured showerheads at 150 W CCP power and 1.5 Torr pressure in SiH_4.

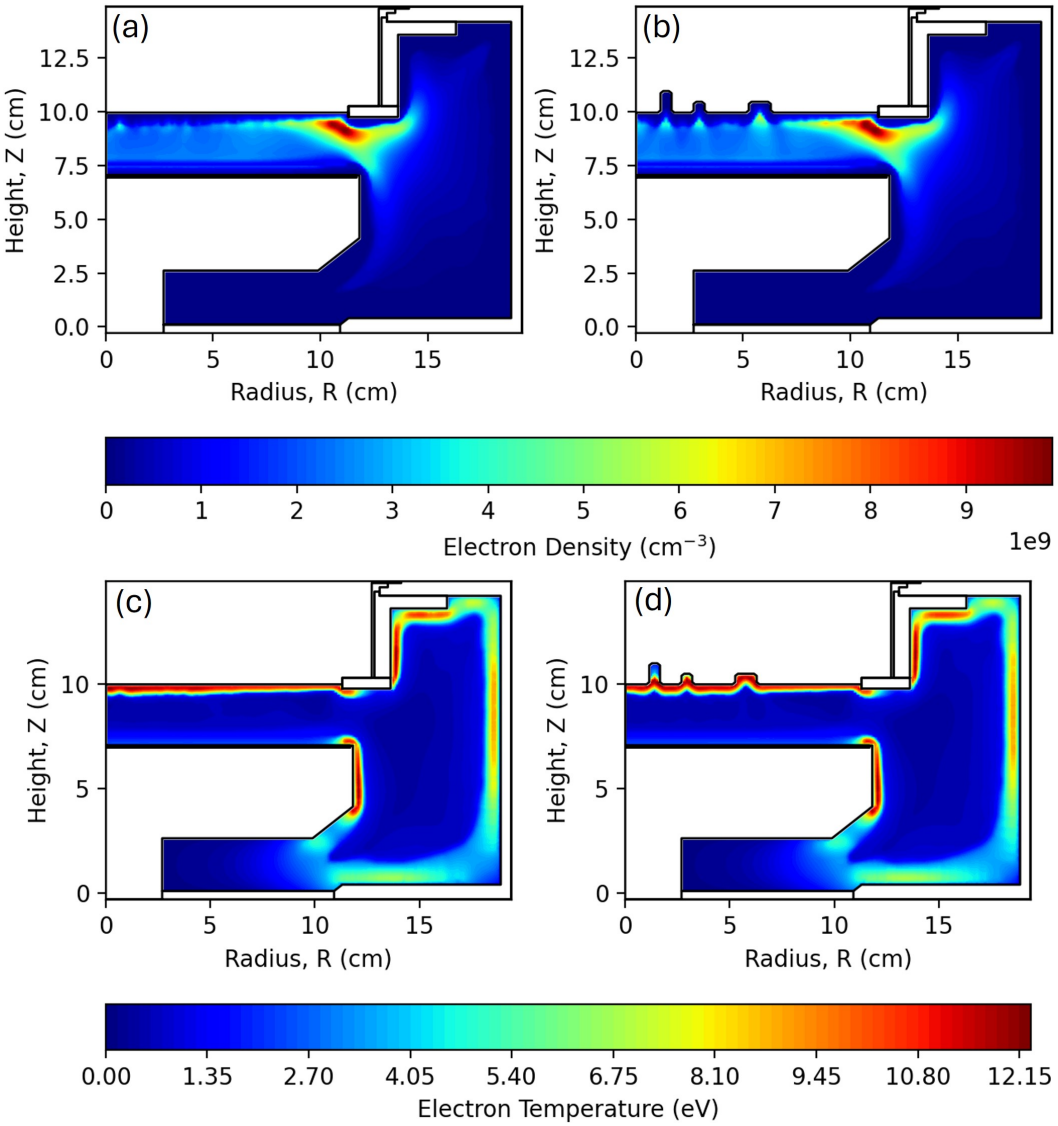

FIG 4. Spatial variation in the electron density and temperature for simulations in SiH_4. Panels (a) and (b) show the electron density for the planar and structured showerhead, respectively. Panels (c) and (d) show the electron temperature for the planar and structured showerhead, respectively. Plasma conditions: 150 W, 1.5 Torr SiH_4.

The planar showerhead electrode, Figure 4 (a), shows a localised region of relatively high electron density of 9.5×10^9 cm^{-3} for radial extents $R = 10 - 11$ cm near to the surface of the electrode, i.e. $Z = 9 - 10$ cm. Elsewhere within the

'bulk' inter-electrode region, the electron density is more uniformly distributed with a lower value of about 2.5×10^9 cm^{-3}, further decreasing to 1.5×10^8 cm^{-3} within the sheath region above the grounded bottom electrode. In contrast, the electron density map in Figure 4 (b) shows that incorporating structured cavities into the powered electrode leads to the formation of spatially localised regions of elevated electron density near to the cavity, e.g. C_1 at $(R, Z) = (1.25, 9)$ cm. This is consistent with previously observed results in Ref. 50 for structured electrode CCPs at 75 mT using argon gas. The local peak density in this region is 4×10^9 cm^{-3}, which is still lower compared to the global peak density observed for both showerhead configurations at the radial edge of the inter-electrode region.

The electron temperature for the planar and structured showerheads, shown in Figure 4 (c) and Figure 4 (d), respectively, shows relatively similar behaviour. The high electron temperatures of 12 eV are observed near the powered showerhead electrode across the full radial extent. Elsewhere in the bulk region, the electron temperature is relatively uniform at a lower value of 1 eV, increasing slightly to 2.5 eV in the region close to the grounded table electrode at $Z = 7$ cm.

2 Density of deposition relevant species: SiH_2, SiH_3 and SiH_3^+

In SiH_4 based deposition processes, neutral radicals such as SiH_2 and SiH_3 possess very high sticking coefficients[1,78]. Moreover, the flux of dominant positive ions like SiH_3^+ leads to the sputtering of the deposited films[79]. Consequently, in such processes, the net film growth is guided by the spatial distribution of key species like SiH_2, SiH_3 and SiH_3^+ [1,78,79]. The simulated densities for these species are shown in Figure 5 for the respective showerhead cases.

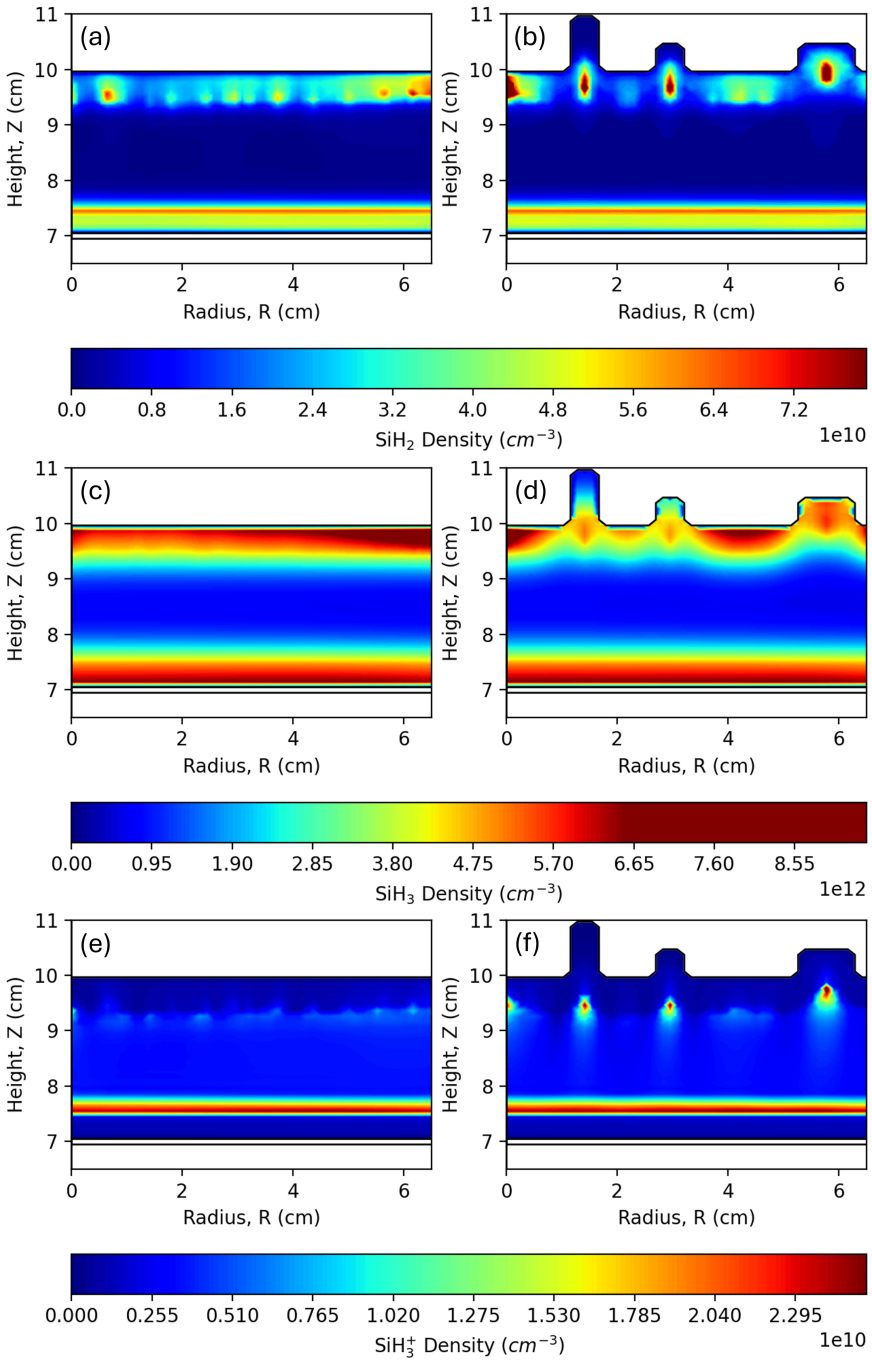

FIG 5. Simulated density of SiH_2, SiH_3 and SiH_3^+ with planar (left) and structured (right) showerheads at 150 W, 1.5 Torr SiH_4. Panels (a) and (b) show SiH_2 density for both cases. Panels (c) and (d) show SiH_3 density for both cases. Panels (e) and (f) show SiH_3^+ density for both cases. Please note the smaller size of the plotted region relative to that of Figure 1.

Figure 5 (a) and Figure 5 (b), respectively, show the density of SiH_2 for the planar and structured showerheads. As for the electron density, shown in Figure 4 (a) and Figure 4 (b), the density of SiH_2 is elevated in the radial location of the cavities, e.g. $9{\times}10^{10}$ cm^{-3} adjacent to cavity C_1 located at $R = 1.25$ cm. For the cavity C_3 located at the largest radial extent, i.e. $R = 5.5$ cm, the localised increase in the density occurs within the cavity, as distinct from C_1 and C_2 that are located nearer to the radial centre and for which the density increases just adjacent to the cavity region, i.e. $Z = 9.5 - 10$ cm. This could be linked to the relatively large cavity width, i.e. 1 cm for C_3 compared to 0.5 cm for C_1 and C_2, which could enable elevated electron temperatures within the cavity as shown in Figure 4 (d). This could further enhance the electron impact reactions, e.g. R21, R23 and R26 (in Table III) within the cavity region, producing high SiH_2 relative to the bulk region. In the region nearby the grounded bottom electrode, i.e. $Z = 7 - 8$ cm, across the full radial extent the density of SiH_2 is observed to be higher relative to the bulk region, reaching $6.5{\times}10^{10}$ cm^{-3} at approximately $Z = 7.5$ cm, and gradually decreases moving towards $Z = 7$ cm. For the planar showerhead case, the electron and SiH_2 density in Figure 4 (a) and Figure 5 (a) show an inhomogeneous spatial profile adjacent to the powered electrode. This could be due to the spatial variation in the electron power deposition, which is 0.1 Wcm^{-3} at the radial centre and 0.4 Wcm^{-3} at the radial edge of the electrode.

Figure 5 (c) and Figure 5 (d), respectively, show the density of SiH_3 for the planar and structured showerhead cases. The planar electrode case shows a relatively uniform density distribution in the radial direction in the region near the powered electrode, i.e. $6{\times}10^{12}$ cm^{-3} for $Z = 9 - 10$ cm compared to $1{\times}10^{12}$ cm^{-3} for $Z = 8 - 9$ cm. As distinct from this, a relatively complicated radial distribution

is observed when a structured showerhead is used, Figure 5 (d). In this case, the SiH_3 density is observed to increase in the region between the cavity structures, e.g. $9{\times}10^{12}$ cm^{-3} between C_2 and C_3 for $R = 3-5$ cm and between the radial centre and C_1, i.e. $R = 0-1$ cm. In the region near the grounded bottom electrode, i.e. $Z = 7-8$ cm, the density of SiH_3 is observed to increase across the full radial extent, reaching a local maxima of $8{\times}10^{12}$ cm^{-3} moving towards $Z = 7$ cm.

Figure 5 (e) and Figure 5 (f), respectively show the density of SiH_3^+ for the planar and structured showerhead cases. The spatial distribution appears to be broadly similar to that observed for SiH_2 in the region near the powered electrode. In the case of SiH_3^+ the density is relatively small, e.g. $2.5{\times}10^{10}$ cm^{-3} for the local maxima adjacent to C_1 at $R = 1.25$ cm in Figure 5 (f) compared to $9{\times}10^{10}$ cm^{-3} in the case of SiH_2, for the same cavity and radial position in Figure 5 (b). These reults suggest that more SiH_3^+ is converted into SiH_2 through electron-impact reaction R21 than produced through ionization reaction R17, as listed in Table III. This can be observed in Figure 5 (f) at cavity C_3, where the SiH_3^+ peak is adjacent to the cavity, whereas, SiH_2 peak is within the cavity in Figure 5 (b). In the region near the grounded bottom electrode, i.e. $Z = 7-8$ cm, an axially localised band of high-density ($3{\times}10^{10}$ cm^{-3}) is observed to be separated from the electrode by a relatively low density ($1.5{\times}10^{9}$ cm^{-3}) region for $Z = 7-7.5$ cm. These observations at the bottom grounded electrode are similar for both the structured and planar showerheads.

For each showerhead type, the density of SiH_2, SiH_3 and SiH_3^+ in the region close to the bottom grounded electrode, i.e. $Z = 7{-}8$ cm, show an almost identical magnitude and spatial distribution. In all cases, the density is elevated compared to the bulk region, i.e. $Z = 8{-}9$ cm. This suggests that the effect of the structured

electrodes on the density of SiH_2, SiH_3 and SiH_3^+ could be primarily localised to the region near the powered electrode, i.e. $Z = 9 - 10$ cm for the intermediate pressure operating conditions.

3 Cavity effects on the radial profile of the flux at the substrate

Figure 6 shows the radial variation in the simulated axial fluxes of SiH_2, SiH_3 and SiH_3^+ to the substrate for the planar and structured showerhead cases. The flux profile of these species on the substrate is similar to the radial density profile of the respective species just above the substrate at $Z = 7.2$ cm. This suggests that the axial velocity of each species across the sheath region is radially uniform.

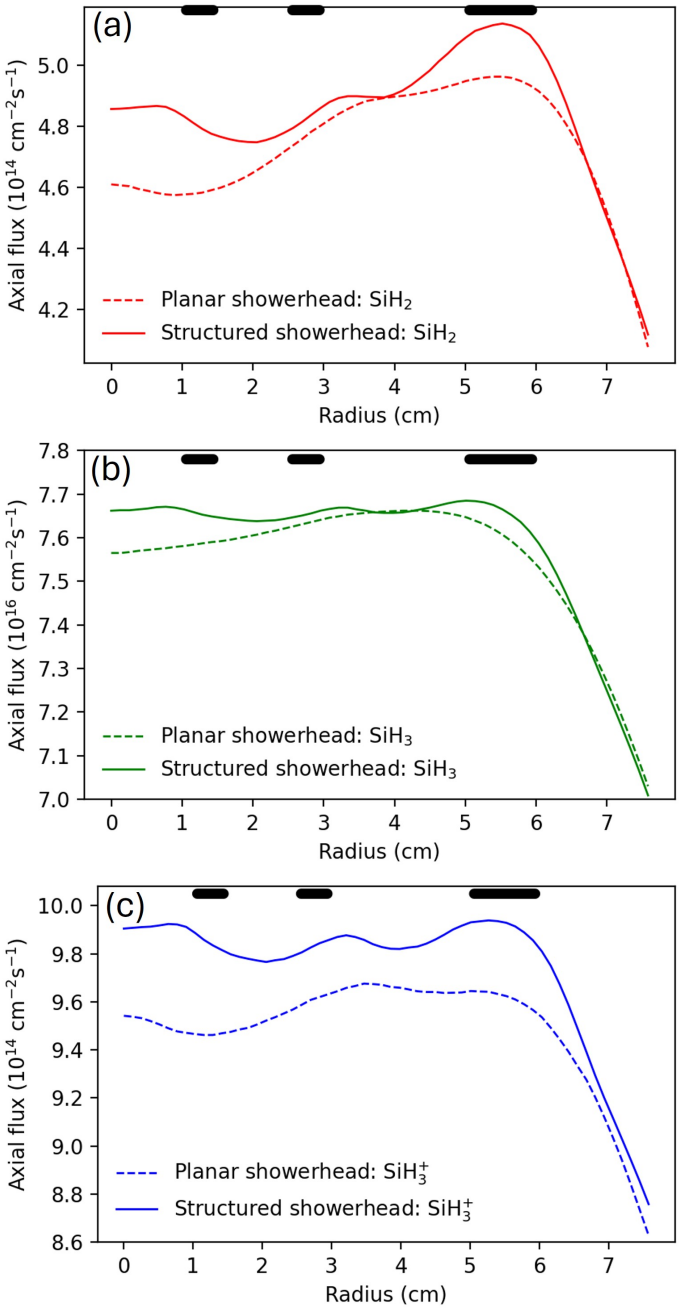

FIG 6. Radial variation in the flux of SiH_2, SiH_3 and SiH_3^+, measured in the axial direction at the surface of the substrate, for the planar and structured showerhead cases. Panel (a) shows the SiH_2 flux, (b) shows the SiH_3 flux and (c) shows the SiH_3^+ flux. The horizontal black lines show the radial extent of the cavities C_1-C_3 that are incorporated into the design of the structured showerhead electrode. Plasma conditions: 150 W, 1.5 Torr SiH_4.

The radial profile in the axial SiH_2 flux, Figure 6 (a), consistently shows higher flux for the structured showerhead case across the radial extent when compared to a planar showerhead. This effect is significant at the radial centre where the fluxes are 4.6×10^{14} $cm^{-2}s^{-1}$ and 4.9×10^{14} $cm^{-2}s^{-1}$, respectively. However, at the radial edge, i.e. for $R > 7$ cm, there is only a marginal difference between the two showerhead configurations. For the structured electrode case, localised peaks in the flux are observed to be approximately correlated with the radial location of the cavities, which could indicate the significance of the peaks in electron density observed to form in similar radial locations in Figure 4 (b).

Furthermore, the radial profiles in the axial SiH_3 and SiH_3^+ flux are shown in Figure 6 (b) and Figure 6 (c) respectively. These observations are qualitatively similar to those of SiH_2 flux in the context of the variations observed for each showerhead case and the localised peaks relative to the cavity locations.

B Thin-film deposition experiments

1 Spatial distribution of thickness and refractive index

Figure 7 shows the spatial variation in SiO_2 film thickness and refractive index for the planar and structured electrode cases measured using ellipsometry.

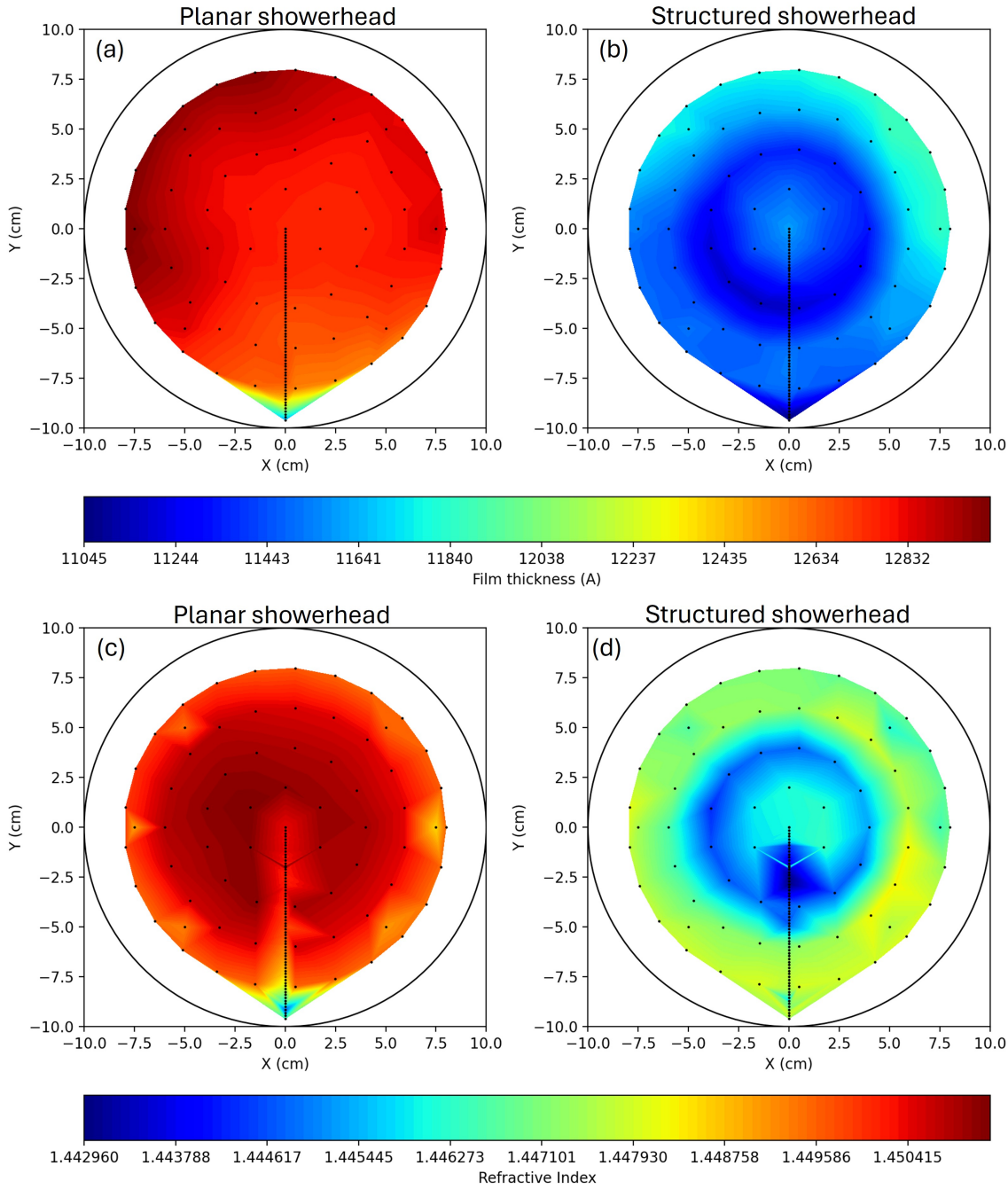

FIG 7. Thickness and refractive index of the deposited SiO_2 films. Panels (a) and (b) show the thickness for the planar and structured showerhead cases, respectively. Panels (c) and (d) show the refractive index for the planar and structured showerhead cases, respectively. Plasma conditions: 150 W, 1.3 Torr $SiH_4/N_2O/N_2$.

The film thickness measurements in Figure 7 (a) and Figure 7 (b) for the respective showerhead cases, shows that the planar geometry produces a thicker film, i.e. 12800 A at the radial coordinates $(X, Y) = (0, 0)$ cm, as compared to 11650 A produced by the structured case. However, near the wafer edge region, i.e. $(X, Y) = (0, -8)$ cm, Figure 7 (a) shows a steep decrease in the thickness profile of a planar case as compared to the structured geometry in Figure 7 (b). Similarly, Figure 7 (c) and Figure 7 (d), shows the refractive index of the resulting films for both cases measured at 632.8nm wavelength. It can be observed that the measured RI for both cases show similar values in the range of 1.4 ± 0.0648, indicating that the spread in RI is minimum and therefore the resulting films have spatially uniform refractive index.

Figure 8 shows the radial thickness profile, which is extracted from the linear ellipsometry measurement pattern described in section II, subsection B, 3 and shown in Figure 3.

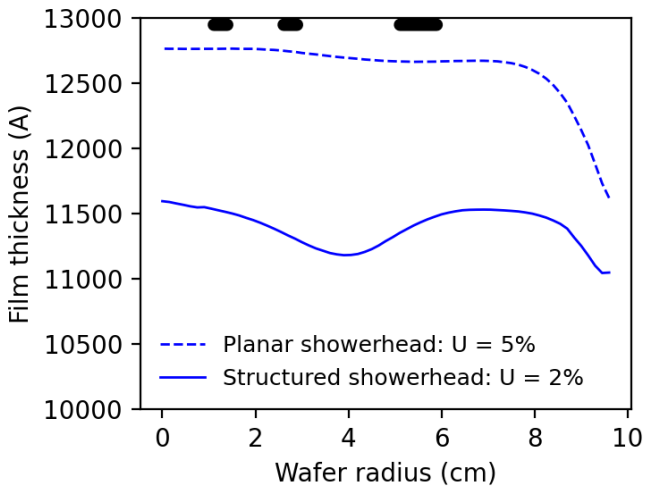

FIG 8. Radial variation in the thickness of the deposited films for the planar and structured showerhead cases. The horizontal black lines show the radial extent of the cavities C_1-C_3 for the structured showerhead electrode. Plasma conditions: 150 W, 1.3 Torr $SiH_4/N_2O/N_2$.

As shown in Figure 8, for the same gas pressure and power level the planar showerhead produces a centre-heavy film thickness profile, whereas the structured geometry gives a radial profile centred around the mean thickness value 11480 A across the full radial extent.

For the case of a planar showerhead, the thickness remains relatively constant, 12800 A up to a radius of about 7.5 cm, which is consistent with a relatively high degree of spatial uniformity when operating with smaller diameter substrates. However, for larger radial extents, i.e. radius beyond 8 cm, there is a substantial fall of 1150 A in the thickness as shown by the dotted curve in Figure 8. This is consistent with a relatively low uniformity in the case of large diameter substrates. As distinct from this, the structured showerhead shows a smaller variation in the thickness profile with respect to the mean value, 11480 A. This could therefore provide a relatively high degree of spatial thickness uniformity when considering the full radial extent. It is important to note that the average film thickness for a structured showerhead is ∼5% lower than that of the planar case. This observation aligns with the higher SiH_3^+ flux shown in Figure 6 (c) for the structured showerhead, resulting in relatively high sputtering of the deposited SiO_2 film. Similarly, for the case of a planar showerhead, high sputtering caused by SiH_3^+ flux in the surrounding region with respect to the centre makes the overall film thickness profile centre-heavy as shown by the dotted line in Figure 8.

2 Impact of the operating pressure on film thickness, refractive index and deposition rate

Figure 9 shows the thickness, refractive index and deposition rate for the planar and structured showerhead electrode cases with respect to gas pressure.

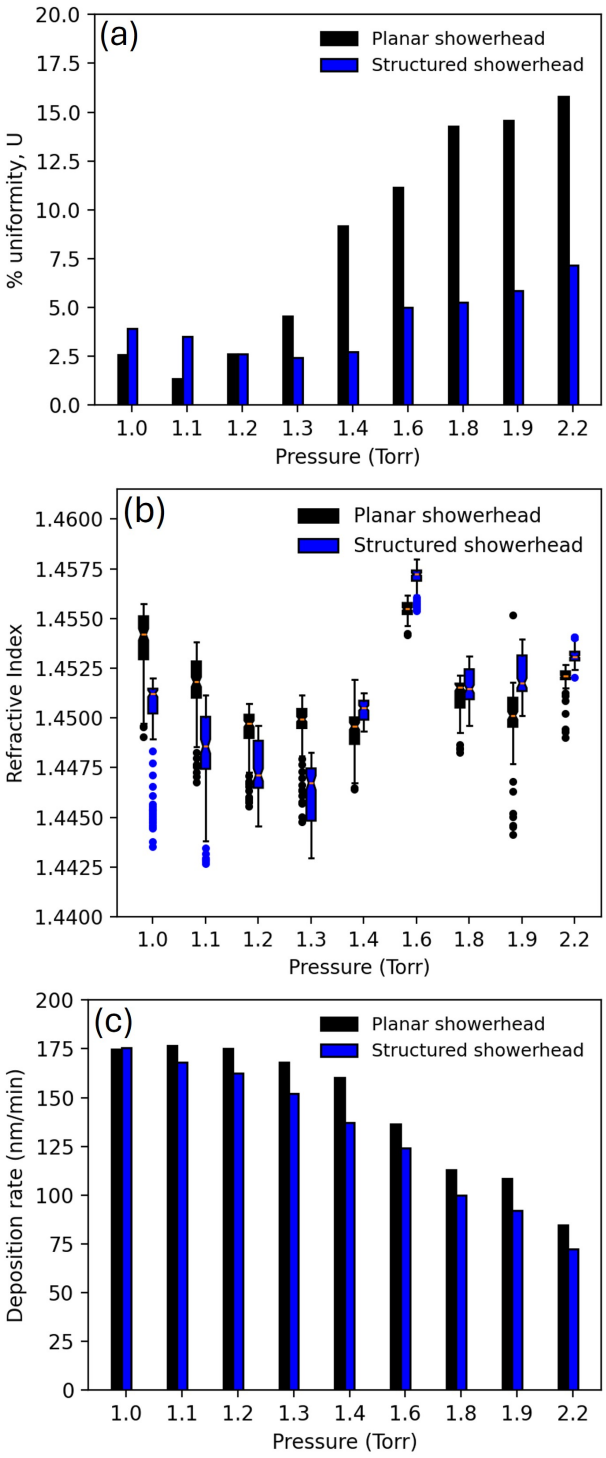

FIG 9. Variation in the (a) film thickness uniformity, (b) refractive index and (c) deposition rate with respect to gas pressure for the planar and structured showerhead cases. Plasma conditions: 150 W, 1-2.2 Torr $SiH_4/N_2O/N_2$.

As shown in Figure 9(a), the film-thickness uniformity for a planar showerhead is sensitive to the gas pressure, and increases from 2.5% at 1 Torr up to 16% at 2.2 Torr. In contrast, the structured showerhead case is relatively insensitive to gas pressure, and the variation in thickness uniformity is from 2.5% to 7% over the same pressure range. The refractive index, shown in Figure 9 (b), is observed to be largely similar for the planar and structured electrode cases between 1-2.2 Torr. The structured showerhead shows a small increase in refractive index for gas pressures above 1.6 Torr and further work is needed to investigate this in detail. The deposition rate, shown in Figure 9 (c), exhibits a similar dependency on the gas pressure for both the structured and planar showerhead geometries. For the full pressure range, the planar showerhead is observed to have a slightly higher rate, e.g. 170 nm/min relative to 150 nm/min for the structured case, at 1.3 Torr. In both cases, the deposition rate remains relatively constant in the pressure range 1-1.2 Torr and gradually decreases with respect to pressure up to 2.2 Torr.

IV CONCLUSION

In the present work, an attempt has been made to infer the SiO_2 film properties based on spatial plasma simulations in pure SiH_4, as most of the deposition process is governed by SiH_4 species. Here, we investigate the impact of introducing annular cavities into the showerhead electrode of a capacitively coupled plasma source used for the deposition of silicon dioxide (SiO_2) thin films. Two-dimensional fluid-kinetic simulations in pure silane show the role of structured cavities in modifying the species concentrations of SiH_2, SiH_3, and SiH_3^+ in the plasma domain, as well as the radial uniformity of the axial flux component of these species onto the table

electrode. Experiments with an industrial plasma enhanced chemical vapour deposition process, operating in $SiH_4/N_2O/N_2$ at 1-2.2 Torr, demonstrate an approximate doubling of the thickness uniformity of the film for a structured showerhead case while maintaining similar values of the refractive index and throughput with respect to the planar showerhead. These results suggest that showerhead electrode designs with structural cavities can potentially be used to increase film-thickness uniformity in intermediate-pressure deposition process reactors.

ACKNOWLEDGMENTS

The authors gratefully acknowledge Thomas Miller, Eleni Apostolopoulou, Kristof Balo, Owain Thomas and Michael Powell from Oxford Instruments Plasma Technology for their support with the experiments, and Andrew R. Gibson from the University of York, and Sebastian Mohr from Quantemol for useful discussions regarding the simulations. This project was supported by Innovate UK under the Knowledge Transfer Partnership programme (KTP-12274).

AUTHOR DECLARATIONS

Conflicts of Interest

The authors have no conflicts to disclose

DATA AVAILABILITY

The data that support the findings of this study can be accessed from the research data repository of the University of York at https://doi.org/10.15124/e0f5da4a-836f-4f56-943b-f65d81964fa5.

REFERENCES

[1] M. A. Lieberman and A. J. Lichtenberg. *Principles of Plasma Discharges and Materials Processing*. Wiley, New York, 2 edition, 2005. doi:10.1002/0471724254.

[2] P. Chabert and N. Braithwaite. *Physics of Radio-Frequency Plasmas*. Cambridge University, Cambridge, 2011. doi:10.1017/CBO9780511974342.

[3] T. Makabe and Z. L. Petrovic. *Plasma Electronics: Applications in Microelectronic Device Fabrication*. CRC, Boca Raton, FL, 2014. doi:10.1201/b17322.

[4] L. A. Berry. *J Fusion Energ*, **12**:365, (1993). doi:10.1007/BF01054814.

[5] H. Takatsuka, M. Noda, Y. Yonekura, Y. Takeuchi, and Y. Yamauchi. *Sol. Energy*, **77**:951, (2004). doi:10.1016/j.solener.2004.06.007.

[6] J P Boeuf. *J. Phys. D: Appl. Phys.*, **36**:R53, (2003). doi:10.1088/0022-3727/36/6/201.

[7] S. Nijdam, K. V. Desai, S. Park, P. P. Sun, O. Sakai, G. Lister, and J. G. Eden. *Plasma Sources Sci. Technol.*, **31**:123001, (2022). doi:10.1088/1361-6595/ac8448.

[8] F. Laermer and A. Urban. *Plasma Process Polym*, **16**:1800207, (2019). doi:10.1002/ppap.201800207.

[9] O. W. Kennedy, J. Sullivan, C. W. Zollitsch, C. N. Thomas, S. Withington, and J. J. Morton. *Mater. Quantum. Technol.*, **1**:045002, (2021). doi:10.1088/2633-4356/AC2EF7.

[10] R. Snyders, D. Hegemann, D. Thiry, O. Zabeida, J. K. Sapieha, and L. Martinu. *Plasma Sources Sci. Technol.*, **32**:074001, (2023). doi:10.1088/1361-6595/acdabc.

[11] S. Bienholz, N. Bibinov, and P. Awakowicz. *J. Phys. D: Appl. Phys.*, **46**: 084010, (2013). doi:10.1088/0022-3727/46/8/084010.

[12] K. A. Alshaltami and S. Daniels. *AIP Advances*, **9**:035047, (2019). doi:10.1063/1.5066286.

[13] D. Eremin, S. Bienholz, D. Szeremley, J. Trieschmann, S. Ries, P. Awakowicz, T. Mussenbrock, and R. P. Brinkmann. *Plasma Sources Sci. Technol.*, **25**: 025020, (2016). doi:10.1088/0963-0252/25/2/025020.

[14] M. A. Lieberman, A. J. Lichtenberg, E. Kawamura, and A. M. Marakhtanov. *Plasma Sources Sci. Technol.*, **24**:055011, (2015). doi:10.1088/0963-0252/24/5/055011.

[15] D. Q. Wen, E. Kawamura, M. A. Lieberman, A. J. Lichtenberg, and Y. N. Wang. *Plasma Sources Sci. Technol.*, **26**:015007, (2017). doi:10.1088/0963-0252/26/1/015007.

[16] K. Zhao, D. Q. Wen, Y. X. Liu, M. A. Lieberman, D. J. Economou, and Y. N. Wang. *Phys. Rev. Lett.*, **122**:185002, (2019). doi:10.1103/PhysRevLett.122.185002.

[17] M A Lieberman, J. P. Booth, P. Chabert, J. M. Rax, and M. M. Turner. *Plasma Sources Sci. Technol.*, **11**:283, (2002). doi:10.1088/0963-0252/11/3/310.

[18] T. Mussenbrock, T. Hemke, D. Ziegler, R. P. Brinkmann, and M. Klick. *Plasma Sources Sci. Technol.*, **17**:025018, (2008). doi:10.1088/0963-0252/17/2/025018.

[19] S. Rauf. *Plasma Sources Sci. Technol.*, **29**:095019, (2020). doi:10.1088/1361-6595/abac4a.

[20] C. H. Kim, H. Kim, G. Park, and H. J. Lee. *Plasma Sources Sci. Technol.*, **30**:065031, (2021). doi:10.1088/1361-6595/ac0a47.

[21] K. Bera, S. Rauf, K. Ramaswamy, and K. Collins. *J. Vac. Sci. Technol. A*, **27**:706, (2009). doi:10.1116/1.3151821.

[22] S. Wilczek, J. Trieschmann, J. Schulze, E. Schuengel, R. P. Brinkmann, A. Derzsi, I. Korolov, Z. Donkó, and T. Mussenbrock. *Plasma Sources Sci. Technol.*, **24**:024002, (2015). doi:10.1088/0963-0252/24/2/024002.

[23] B. G. Heil, U. Czarnetzki, R. P. Brinkmann, and T. Mussenbrock. *J. Phys. D: Appl. Phys.*, **41**:165202, (2008). doi:10.1088/0022-3727/41/16/165202.

[24] S. B. Wang and A. E. Wendt. *J. Appl. Phys.*, **88**:643, (2000). doi:10.1063/1.373715.

[25] P. Diomede, D. J. Economou, and V. M. Donnelly. *J. Appl. Phys.*, **109**: 083302, (2011). doi:10.1063/1.3573488.

[26] D. Sung, S. Jeong, Y. Park, V. N. Volynets, A. G. Ushakov, and G. H. Kim. *J. Vac. Sci. Technol. A*, **27**:13, (2009). doi:10.1116/1.3010717.

[27] K. Bera, S. Rauf, and K. Collins. *IEEE Trans. Plasma Sci.*, **36**:1366, (2008). doi:10.1109/TPS.2008.924413.

[28] T. Lafleur. *Plasma Sources Sci. Technol.*, **25**:013001, (2015). doi:10.1088/0963-0252/25/1/013001.

[29] A. R. Gibson, A. Greb, W. G. Graham, and T. Gans. *Appl. Phys. Lett.*, **106**: 054102, (2015). doi:10.1063/1.4907567.

[30] P. C. Boyle, A. R. Ellingboe, and M. M. Turner. *J. Phys. D: Appl. Phys.*, **37**: 697, (2004). doi:10.1088/0022-3727/37/5/008.

[31] A. C. Wu, M. A. Lieberman, and J. P. Verboncoeur. *J. Appl. Phys.*, **101**: 056105, (2007). doi:10.1063/1.2435975.

[32] Y. R. Zhang, S. Tinck, P. D. Schepper, Y. N. Wang, and A. Bogaerts. *J. Vac. Sci. Technol. A*, **33**:021310, (2015). doi:10.1116/1.4906819.

[33] P. Hartmann et al. *Plasma Sources Sci. Technol.*, **29**:075014, (2020). doi:10.1088/1361-6595/ab9374.

[34] E. V. Johnson, T. Verbeke, J. C. Vanel, and J. P. Booth. *J. Phys. D: Appl. Phys.*, **43**:412001, (2010). doi:10.1088/0022-3727/43/41/412001.

[35] P. Hartmann et al. *J. Phys. D: Appl. Phys.*, **54**:255202, (2021). doi:10.1088/1361-6463/abf229.

[36] S. Brandt et al. *Plasma Sources Sci. Technol.*, **25**:045015, (2016). doi:10.1088/0963-0252/25/4/045015.

[37] P. Chabert, J. L. Raimbault, J. M. Rax, and A. Perret. *Phys. Plasmas*, **11**: 4081, (2004). doi:10.1063/1.1770900.

[38] H. Schmidt, L. Sansonnens, A. A. Howling, C. Hollenstein, M. Elyaakoubi, and J. P. Schmitt. *J. Appl. Phys.*, **95**:4559, (2004). doi:10.1063/1.1690096.

[39] L. Sansonnens and J. Schmitt. *Appl. Phys. Lett.*, **82**:182, (2003). doi:10.1063/1.1534918.

[40] Y. Takeuchi, Y. Nawata, K. Ogawa, A. Serizawa, Y. Yamauchi, and M. Murata. *Thin Solid Films*, **386**:133, (2001). doi:10.1016/S0040-6090(00)01663-1.

[41] Y. Yang and M. J. Kushner. *J. Phys. D: Appl. Phys.*, **43**:152001, (2010). doi:10.1088/0022-3727/43/15/152001.

[42] T. Lafleur, P. Chabert, and J. P. Booth. *J. Phys. D: Appl. Phys.*, **46**:135201, (2013). doi:10.1088/0022-3727/46/13/135201.

[43] L. Wang, P. Hartmann, Z. Donkó, Y. H. Song, and J. Schulze. *Plasma Sources Sci. Technol.*, **32**:045002, (2023). doi:10.1088/1361-6595/acc6e9.

[44] L. Wang, P. Hartmann, Z. Donkó, Y. H. Song, and J. Schulze. *Plasma Sources Sci. Technol.*, **34**:045004, (2025). doi:10.1088/1361-6595/adc504.

[45] Y. Ohtsu and H. Urasaki. *Plasma Sources Sci. Technol.*, **19**:045012, (2010). doi:10.1088/0963-0252/19/4/045012.

[46] Y. Ohtsu and Y. Kawasaki. *J. Appl. Phys.*, **113**:033302, (2013). doi:10.1063/1.4776220.

[47] Y. Ohtsu and N. Matsumoto. *J. Vac. Sci. Technol. A*, **32**:031304, (2014). doi:10.1116/1.4871467.

[48] Y. Ohtsu, N. Matsumoto, J. Schulze, and E. Schuengel. *Phys. Plasmas*, **23**: 033510, (2016). doi:10.1063/1.4943964.

[49] N. Schmidt, J. Schulze, E. Schüngel, and U. Czarnetzki. *J. Phys. D: Appl. Phys.*, **46**:505202, (2013). doi:10.1088/0022-3727/46/50/505202.

[50] L. Wang, P. Hartmann, Z. Donkó, Y. H. Song, and J. Schulze. *J. Vac. Sci. Technol. A*, **39**:063004, (2021). doi:10.1116/6.0001327.

[51] J. K. Joshi, S. K. Karkari, and S. Kumar. *IEEE Trans. Plasma Sci.*, **47**:5291, (2019). doi:10.1109/TPS.2019.2952160.

[52] S. Dahiya, P. Singh, Y. Patil, S. Sharma, N. Sirse, and S. K. Karkari. *Phys. Plasmas*, **30**:093505, (2023). doi:10.1063/5.0160506.

[53] I. Korolov, A. Derzsi, Z. Donkó, and J. Schulze. *Appl. Phys. Lett.*, **103**: 064102, (2013). doi:10.1063/1.4817920.

[54] M. H. Islam and Y. Ohtsu. *J. Vac. Sci. Technol. A*, **43**:043007, (2025). doi:10.1116/6.0004690.

[55] S. J. Doyle, T. Lafleur, A. R. Gibson, P. Tian, M. J. Kushner, and J. Dedrick. *Plasma Sources Sci. Technol.*, **26**:125005, (2017). doi:10.1088/1361-6595/aa96e5.

[56] T. Lafleur and R. W. Boswell. *Phys. Plasmas*, **19**:023508, (2012). doi:10.1063/1.3685709.

[57] M. J. Kushner. *J. Phys. D: Appl. Phys.*, **42**:194013, (2009). doi:10.1088/0022-3727/42/19/194013.

[58] See *Quantemol Virtual Tool* at. URL https://quantemol.com/quantemol-vt/.

[59] C. E. Huerta and R. E. Wirz. *AIP Advances*, **9**(12):125009, (2019). doi:10.1063/1.5120519.

[60] J. Tennyson et al. *Plasma Sources Sci. Technol.*, **31**:095020, (2022). doi:10.1088/1361-6595/ac907e.

[61] M. Hayashi. *J. Phys. Colloques*, **40**:C7, (1979). doi:10.1051/jphyscol:1979722.

[62] R. K. Janev, W. D. Langer, D. E. Post, and K. Evans. *Elementary Processes in Hydrogen-Helium Plasmas*. Springer, Berlin, Heidelberg, 2012. doi:10.1007/978-3-642-71935-6.

[63] D. A. Vroom and F. J. Heer. *J. Chem. Phys.*, **50**:580, (1969). doi:10.1063/1.1671103.

[64] S. J. Choi and M. J. Kushner. *Appl. Phys. Lett.*, **62**:2197, (1993). doi:10.1063/1.109440.

[65] C. F. Chan, C. F. Burrell, and W. S. Cooper. *J. Appl. Phys.*, **54**:6119, (1983). doi:10.1063/1.331948.

[66] M. J. Kushner. *J. Appl. Phys.*, **63**:2532, (1988). doi:10.1063/1.340989.

[67] T. Gougousi, R. Johnsen, and M.F. Golde. *Int. J. Mass Spectrom.*, **149**:131, (1995). doi:10.1016/0168-1176(95)04248-J.

[68] L. E. Kline. *IEEE Trans. Plasma Sci.*, **10**:224, (1982). doi:10.1109/TPS.1982.4316180.

[69] J. Perrin, O. Leroy, and M. C. Bordage. *Contrib. Plasma Phys.*, **36**:3, (1996). doi:10.1002/ctpp.2150360102.

[70] E. Meeks, R. S. Larson, P. Ho, C. Apblett, S. M. Han, E. Edelberg, and E. S. Aydil. *J. Vac. Sci. Technol. A*, **16**:544, (1998). doi:10.1116/1.581096.

[71] I. Méndez, I. Tanarro, and V. J. Herrero. *Phys. Chem. Chem. Phys.*, **12**:4239, (2010). doi:10.1039/B925202A.

[72] A. P. Hickman. *J. Chem. Phys.*, **70**:4872, (1979). doi:10.1063/1.437364.

[73] H. Chatham and A. Gallagher. *J. Appl. Phys.*, **58**:159, (1985). doi:10.1063/1.335702.

[74] E. R. Austin and F. W. Lampe. *J. Phys. Chem.*, **81**:1134, (1977). doi:10.1021/j100527a003.

[75] C. Tian and C. R. Vidal. *J. Phys. B: At. Mol. Opt. Phys.*, **31**:895, (1998). doi:10.1088/0953-4075/31/4/031.

[76] W. V. Gaens and A. Bogaerts. *J. Phys. D: Appl. Phys.*, **46**:275201, (2013). doi:10.1088/0022-3727/46/27/275201.

[77] See *Oxford Instruments PlasmaPro 100 PECVD* at. URL https://plasma.oxinst.com/products/pecvd/plasmapro-100-pecvd.

[78] M. J. McCaughey and M. J. Kushner. *J. Appl. Phys.*, **65**:186, (1989). doi:10.1063/1.342568.

[79] D. Smith. *Thin-Film Deposition: Principles and Practice*. McGraw Hill, New York, 1995.